MICOS Complex and Mitochondria Morphology Changes Across Aging in Cardiac Muscle 3D Reconstructions

Zer Vue[1,*], Kit Neikirk[1,*], Larry Vang[1,*], Edgar Garza-Lopez[2], Heather K. Beasley[1], Andrea G. Marshall[1], Sandra A. Murray[3], Antentor Hinton, Jr[1,#]

Affiliations:
[1] Department of Molecular Physiology and Biophysics, Vanderbilt University, Nashville, TN, 37232, USA
[2] Department of Internal Medicine, University of Iowa, Iowa City, IA, 52242, USA.
[3] Department of Cell Biology, School of Medicine, University of Pittsburgh, Pittsburgh, PA, 15260, USA.

ABSTRACT: Cardiac disease remains a large cause of death among humans and therapies to treat it remain lacking. Mitochondria is heavily implicated in various critical functions of the cell not limited to the production of ATP. Critically, mitochondria break down across aging and heart also decrease in efficiency in aging. Key factors implicated in mitochondria morphology, such as the mitochondrial contact site and cristae organizing system (MICOS), role across aging remains to be seen in cardiac muscle. To better understand the relationship between mitochondria in heart, we used transmission electron microscopy (TEM) and serial block facing-scanning electron microscopy (SBF-SEM) to quantitatively analyze the 3D networks in cardiac muscle samples of mice at aging intervals. Cardiac muscle showed some breaking down across aging, decreased areas, increased mitochondria, but less fragmentation and wide-spread changes across 2-year aging than previous studies in skeletal muscle. In studying cristae, the inner folds of mitochondria, we observed a loss of morphology across aging. This mimicked what was observed upon CRISPR/Cas9 knockdown of *mitofilin, Chchd3, Chchd6* and *Opa-1* which showed poorer quality cristae and fragmented mitochondria while mitochondria length and volume decreased. We are the first to examine mitochondria changes in cardiac muscle across aging. Notably, we noticed differences in skeletal muscle, which we have previously studied, and cardiac muscle that suggests a differential response to mitochondrial aging in cardiac and skeletal muscle. In combination, these data suggest that, in the heart, loss of the MICOS complex may be implicated in the loss of function in mitochondria that is seen across aging.

INTRODUCTION:

The mitochondria is an organelle that critically carries out oxidative phosphorylation in the cell, and is implicated in many disease states including Alzheimer's, diabetes, and heart failure [1–3]. Given the dependence on mitochondria for the energy, deterioration or loss of function in mitochondria can be associated with failure of cells and states including autophagy, in some cases, and apoptosis [4–6]. Beyond only being responsible for producing adenosine triphosphate (ATP), mitochondria also are involved in cell signaling, through calcium homeostasis; programmed cell death, apoptosis; and regulate immunity, through signaling that determines immune cell function [5,7–9]. Interestingly, previous research has also suggested that mitochondria is implicated in aging [10,11]. The mitochondrial free radical theory of aging

(MRFTA) proposes this mechanism arises as a result of degradation by of reactive oxygen species, which are oxidative phosphorylation byproducts [10,12]. While many of the functions of mitochondria have been studied before, the specific changes and causes of changes in mitochondria across aging is still poorly understood, as is how this could be linked to disease states.

Key to mitochondria function is the morphology. Mitochondria undergo dynamics of fusion and fission which are regulated by optic atrophy 1 (OPA-1) and dynamin related protein-1 (DRP-1), respectively [4,13–15]. While loss of DRP-1 results in an abundance of mitochondria that fuse together and are overly elongated [5], loss of OPA-1 results in mitochondria that are fragmented [13,16]. Beyond this, loss of either of these critical genes also impact mitochondrial cristae [14,17]. Cristae are folds of the mitochondria inner-membrane that have electron transfer chain complexes which are responsible for ATP synthesis [18]. Critically, the morphology of cristae can be critical in their energetic efficiency [18]. Beyond this, cristae morphology has also been implicated in other functions of mitochondria [18]. For cristae, the shape can present different outcomes in mitochondria, and cristae can be seen as either lamellar, during which they present as flat sacs, or tubular, during which they resemble tubes [19]. Typically, cristae dynamically have populations of both lamellar and tubular cristae. However, recent research has suggested that lamellar cristae does not require mitochondrial fusion, so therefore they may be able to form independent of OPA-1, or in states of OPA-1 deficiency [20]. Lamellar cristae is more accommodating of increases in volume, and have been suggested that they increase in prominence as cristae fusion occurs during mitochondria stress states [21].

Critical in the regulation of both of these formations of cristae types is the mitochondrial contact site and cristae organizing system (MICOS). Similar to OPA-1, the MICOS complex regulates changes in the cristae, as cristae show continuous changes [17,22–24]. The MICOS complex is made up of several key genes that are critical in maintaining the morphology of both cristae and mitochondria [24]. Beyond only regulating the shape of cristae, maintenance of junctions in the cristae, which act as sub compartments for mitochondria as barriers for metabolites, is also controlled by the MICOS complex [25]. Given the importance of the cristae junctions, this may also implicate cristae in calcium homeostasis and molecular signaling. Given the implication of mitochondria and cristae morphology in function, alterations in the MICOS complex could further impact health [23]. Specifically, it remains unknown how the MICOS complex affects aging and mitochondria health in the heart. Given past research that has suggested mitochondria is affected by aging [11], we hypothesized that this change may come as a result of changes in the MICOS complex, which are critical to maintaining mitochondrial and cristae morphology [20,26].

We have specifically sought to study cardiac muscle in mouse because it remains a novel target that has implications for mitochondria health of the heart. This study combines an *in vivo* and *in vitro* approach by both looking at cardiac muscle in mouse and fibroblasts. Previously, aging has been studied in cardiomyocytes [27]; however, these studies have not considered the MICOS complex in relation to this aging of the cardiomyocytes. Cardiac health is heavily implicated with insulin-resistance and is linked to diabetes [1,28]. Importantly, heart failure has also been linked to factors including endoplasmic reticulum stress, mitochondrial bioenergetics, insulin signaling, autophagy, and oxidative stress [29], which are all factors the mitochondria plays a role in [6,30–32]. Mitochondria show specialization in types and structures associated with their roles in glycolysis and oxidative metabolism in cardiomyocytes [33–36]. While young mitochondria show extensive specialization, it is not known whether this is true for aged mitochondria, there is

little information on whether the impact of aging regulates mitochondrial genes that affect structure. In cardiac muscle, past research has found that across aging, mitochondria in between myofibrils, called interfibrillar mitochondria, show the largest decrease in mitochondria function [37]. However, it remains to be seen what caused these changes in the oxidative phosphorylation of interfibrillar mitochondria. Given that heart failure increases across aging as heart function is loss [38], mitochondria may contribute to this [29]. Therefore, mitochondria in the heart represent a critical target for therapies aimed at cardiac diseases, heart failure, and diabetes.

To better understand the relationship between mitochondria in heart, we used transmission electron microscopy (TEM) for 2D micrographs to observe mitochondria, cristae, and lipids. We also used serial block facing-scanning electron microscopy (SBF-SEM) to quantitatively analyze the 3D networks in cardiac muscle samples of mice at aging intervals. With this high-resolution technique, we were able to look at single-organelle resolution and compared shape, morphology, amount, networking, and branching across age points. To further understand how aging affected the morphology, we looked at mitochondria and cristae at three time points, 3-month, 1-year, and 2-year which represent "young," "middle-aged," and "old," mouse respectively. We have previously performed this method in skeletal muscle. Previous research has shown that cardiac and skeletal muscle differ [33,34], but this is not yet known how this changes across aging. Furthermore, we also looked at the impact of aging in MICOS genes. Critically, in this study, we used CRISPR/Cas9 editing to individually knockout (KO) three genes of the MICOS complex, and *Chchd3* (*Mic19*), *Chchd6* (*Mic25*), *Mitofilin* (*Mic60*), as well as *Opa-1* and examined mitochondria through fluorescence and 3D reconstruction. Finally, we also observed KO of the MICOS complex genes and *Opa-1* through 3D reconstruction in cardiac fibroblasts.

RESULTS:

TEM Shows Changes in Mitochondria and Cristae Across Aging

While it is commonly understood that cardiac heart declines across age, we sought to further establish this in a mouse model. To begin with, we wanted to understand how heart characteristics change in mice across aging. Echometric data shows changes across aging included reduced heart rate and increased cardiac output (Supplementary Figure 1). As expected, mice increased in body weight across their aging (Figure 1A). However, importantly fat mass increased at a much higher rate than lean mass, especially in the 2-year sample (Figure 1B-C). Heart mass also significantly increased across aging (Figure 1D). The glucose tolerance test showed that aged mice had a greater reaction to mitochondria (Figure 1E). In tandem, these results suggest that across aging mice has higher fat contents and weaker adaptive responses. However, to further explore these roles, TEM was necessary to understand mitochondria and cristae morphology.

We began by examining mitochondria and cristae morphology in cardiac muscle across 3-month, 1 year, and 2-year-old mouse. Studying cardiac muscle allows if mitochondria morphological changes are exclusive to skeletal muscle, since cardiac muscle allows for the comparison to different types of cells [36], and cardiac muscle can give information about potential causes of loss of optimal function in heart across aging [38]. TEM is useful as it gives very high quality micrographs which allow for viewing of cristae and identification of mitochondria [39]. While the young male mouse show very clearly mitochondria with electron dense membranes

and clear membranes, the aged mouse show less clear mitochondria and cristae (Figure 1F-F''). Mitochondria number more than quadruples from the 3-month to 1-year sample, before slightly leveling out from 1-year to 2-year (Figure 1G). Although mitochondria are increased, an inverse effect is seen for mitochondria area as the average is significantly smaller in samples that are older than 3-month; although the decrease is smaller between the 1-year and 2-year sample (Figure 1H). The mitochondria also became slightly more circular (Figure 1I). To measure cristae, the inner-folds, first cristae numbers in each mitochondria was evaluated (Figure 1J). This showed that cristae numbers decreased across aging, consistently (Figure 1J). Finally, cristae score was used to access cristae of mitochondria. Cristae score is a holistic method to evaluate cristae based on both their quantity and morphology [39,40]. A cristae score of 0 represents no clearly defined cristae, while a cristae of 2 represents that less than 75% of mitochondria have cristae, and a maximum cristae score of 4 represents many regular cristae. Across aging in cardiac muscle, again there was a large drop off in the quality of cristae. The young 3-month sample ranged between mostly regular cristae with some irregular, with cristae scores of about 3.3. The aged samples both have cristae score around 2, which shows there is much area lacking cristae or having irregular cristae (Figure 1K).

We further analyzed these changes in a female-aged mouse model, as previous studies have shown sex-dependent differences in mitochondrial morphology [41] (SFigure 2A-A''). Across aging, mitochondria similarly showed fragmentation as they increased in number while decreasing in area (SFigure 2B-C). The mitochondria further became more circular (SFigure 1D). Cristae also underwent similar changes as they became less defined, reduced in amount, and their score decreased (SFigure 2E-F). In tandem, these results suggest that sex-dependent differences do not occur across aging in mitochondrial structure in cardiac muscle.

Since mitochondrial and cristae quality is decreased, we theorized there may be an alternative mechanism for energy. The 1-year and 2-year representative images of mitochondria show many lipid droplets near mitochondria (orange arrows, Figure 1F-F'') which suggest lipid formation as a response to mitochondria stress.[42] Therefore, we stained for lipids in the 3-month and 2-year (Figure 1L-L'). Similar to mitochondria, we observed a large increase in lipid number, but the lipid droplet formations were much smaller (Figure 1M-N).

Together, these data suggested that mitochondrial fission increased and cristae regulation decreased across aging; however, TEM can be limiting in analyzing changes of mitochondria. Therefore, we moved to a more complex 3D reconstruction in a male model.

Aging Changes Mitochondria and MERC Morphology in Cardiac Muscle

From there, we sought to determine how aging alters mitochondrial networks and individual mitochondria. We imaged cardiac muscle biopsies from young (3-month-old), mature (1-year-old) and aged (2-year-old) mice by SBF-SEM. While SBF-SEM does not allow for proper viewing of cristae, with resolutions of 10 µm for the x- and y- planes and 50 µm for the z-plane, it allows visualization of the electron connectome [16]. Importantly, it also allows for 3D reconstruction of mitochondria, which more accurately represent how mitochondria exist in 3D space, than 2D methods. We specifically examined the changes of morphology in the intermyofibrillar (IMF) region [43]. While past research has found frequency of mitochondria increases in this reason, further elucidation is needed to show if aging in cardiac muscle changes mitochondria orientation, C-band sarcomeres of myofibrils, or other changes, such as the formation of nanotunnels. We surveyed 175 IMF mitochondria from each of the three mice (n=3) sampled at each time point for SBF-SEM for a total of 500 mitochondria for each age cohort.

From there, at 50 µm intervals at the transverse intervals, 300 slices, known as orthos, were sectioned. Given the 10 µm by 10 µm resolution of image stacks, we surveyed approximately 50 IMF mitochondria from each stack.

To begin with analyzing the size and shape of mitochondria, we showcase the orthoslice of the mitochondria showing representative SEM of cardiac muscle (Figure 2A-C), the overlay of the 3D reconstruction (Figure 2A'-C'), and the isolated 3D reconstruction to allow for better viewing of the structure (Figure 2A''-C''). We found that there was a significant decrease in perimeter, and volume between the 3 month and 1-year cohorts (Figure 2D-F). In the case of perimeter, 3D area, and volume there was another decrease going from 1-year to 2-year which was a larger increase than the initial decrease in from 3-month (Figure 2D-F). However, in all cases this decrease was less than the decrease present in skeletal muscle we have previously found. Importantly, while the volumes, 3D area, and perimeter of skeletal muscle has previously been shown to be decreased heavily across aging, especially in the 2-year sample, a similar effect was not observed for cardiac muscle (Figure 2D-F). For each of these quantifications, 3 individual mice were sampled at each of the three time points (SFigure 3A-C). When looking at the quantifications of individual mice, most mice were similar and demonstrated a small downward trend, although in some cases the 1-year individuals had higher volume, perimeter, and area than the 3-month young individuals. This suggests that although some mitochondria morphology is loss across aging, less fragmentation has occurred than expected and compared to other types. From there, we sought to understand if networks of mitochondria changed in response to aging.

To further characterize the changes of cardiac muscle, we looked at them from both a transverse (Figure 3A-C) and longitudinal view (Figure 3A'-C'). They showcased packed together, smaller mitochondria which did not have any significant network formations visible. To further characterize the mitochondrial types of each age cohort, we did mito-otyping, which is a method similar to karyotyping to organize mitochondria on the basis of their volumes to better categorize the diversity of the mitochondria (Figure 3D). This allows for comparison of the mitochondria across age at each volume. Critically, it showed that volumes did not have significant changes across all ages, nor did it seem complexity. Furthermore, the decrease in sphericity for cardiac muscle was very small (Figure 3E), so the sphericity barely changed across aging. To understand the networking of mitochondria better, we utilized mitochondrial branching index (MBI). The mitochondrial branching index has been used in the past as a measure of complexity by examining the ratio between transverse and latitude mitochondria [36]. MBI showed that complexity decreased across aging, with the largest decrease occurring from 3-month to 1-year.

Similarly, looking at the individual mice for each of the age cohorts, it seems that there is no significant variation between mice, but there was a large amount of heterogeneity in mitochondria samples in each mouse (SFigure 4A-B). In contrast, we have previously found there was a small increase in skeletal muscle sphericity. This suggests that complexity does not significantly increase in cardiac muscle. In combination, the aged cardiac muscle mitochondria resembled healthy mitochondria with a lack of phenotyping or fragmenting present (Figure 3). We further found that in the heart model, in contrast to the skeletal muscle we have previously studied, mitochondria do not develop nanotunnels (Figure 3). While these studies showed mitochondria that managed to maintain their morphology across aging, from there we sought to understand what effects loss of the MICOS complex have on cardiac muscle.

Loss of MICOS Complex Genes across Aging and 3D reconstruction Reveals a Change in Morphology and Oxygen Consumption Rate upon their Knockout in Fibroblast

Although it is established that the MICOS complex is critical in mitochondrial dynamics [24,26], the relation to aging requires further elucidation. Previously, *Opa-1* has in the past been found to be decreased across aging [44]. Furthermore, in skeletal muscle we have previously found that *Opa-1, Mitofilin, Chchd3,* and *Chchd6* significantly decreased across aging; however, we sought to see if the MICOS complex gene transcripts also decreased in cardiac muscle. We found that, as previous research has observed [44], *Opa-1* decreased by over 50% across 2-years compared to the 3-month sample (Figure 4A). *Mitofilin* had a similarly drastic change as the 2-year gene transcript amounts were less than 50% of the 3-month sample (Figure 4B). *Chchd3* and *Chchd6* both also showed a progressive decrease across time, although their levels did not decrease as much as other transcripts (Figure 4C-D). To further understand the role of mitochondrial dynamics upon the loss of these MICOS genes, we knocked them out in fibroblast cells.

Specifically, we measured 1250 mitochondria across 10 cells. Since it is already known that loss of *Opa-1* results in changes in morphology [13,16,17,39], it was a positive control for mitochondrial morphology changes. To begin with, we marked mitochondria with MitoTracker Red and used confocal fluorescence to look to examine mitochondria and verify successful knocking out of *Opa-1, Mitofilin, Chchd3,* and *Chchd6* (Figure 5A). From there, SBF-SEM reconstruction was performed of mitochondria of each of the knockout fibroblasts (Figure 5A-D). From there, we performed quantifications for each of the KO models. We saw significant decreases in mitochondria length upon all of the knockouts of the MICOS complex and *Opa-1* (Figure 5B). Similarly, there were also very large decreases in the volume of mitochondria (Figure 5C). This suggests an uptick in fission potentially in combination with decreased fusion. This is further supported by the much higher percentage of mitochondria that are fragmented (Figure 5D). Notably, *Chchd3* is nearly completely fragmented, similar to *Opa-1*. We further sought to quantify if the mitochondria were more tubular or lamellar, which represents stressed states. We found that while the wildtype was mostly lamellar, all the KO models were much more tubular, with the most tubular being *Opa-1* and *Chchd3*. We further employed live dynamics confocal imaging to see the mitochondria in real time, as opposed to a static state. The wildtype mitochondria (Video 1) showed typical mitochondria, potentially undergoing fusion. However, the KD of *OPA1* (Video 2), *Chchd3* (Video 3), and *mitofilin* (Video 4), all showed fragmented mitochondria. In combinations, these finds show clear fragmentation and stress states occurring in mitochondria upon the loss of any of the genes associated with the MICOS complex.

However, while previous research has shown that mitochondria fragmentation results in reduced oxygen consumption [45]. To verify this, we measured oxygen consumption race (OCR) using an XF24 extracellular flux bioanalyzer upon knockout of OPA1 and MICOS genes in fibroblasts. For *OPA1* and *mitofilin* KD, basal OCR, ATP-linked OCR, and maximum OCR all decreased compared to a control (Figure 5E-H). This shows a general loss in the function of the mitochondria. However, for reserve capacity OCR, interestingly *mitofilin* KD slightly increased compared to *OPA1* KD which showed a sharp decline (Figure 5I). For CHCHD3 and CHCHD6 KD, there was a sharp decrease of basal OCR, ATP-linked OCR, maximum OCR, and reserve capacity OCR (Figure 5J-N). These, in tandem, suggest impairment of the electron transfer chain. The changes in morphology of aging mice could be further influenced by the loss of the

MICOS genes. However, to further understand the specific pathways altered upon aging, we used metabolomic analysis.

Metabolomic Analysis of Mice Across Aging

To better understand what caused the changes across aging we observed, we compared metabolites in 3-month versus 2-year mice. Metabolite principal component analysis (PCA) was employed to find the main axes of differences between 3-month and 2-year sample, and revealed distinct differences existed (Figure 6A). From there, T-tests allowed for finding peaks which were upregulated in the and 2-year mice (Figure 6B). Importantly, a heatmap was constructed showing the relative abundance of ions in 3-month versus 2-year mice (Figure 6C). Several key classes showed marked decrease in the 2-year samples methionine and serine, while other classes increased in the 2-year sample, including pantothenic acid and pentadecanoic acid. To further explore the specific, this, several key pathways included fatty acid and folate metabolism were upregulated in 2-year mice (Figure 6D). Similarly, a volcano plot showed that malonate and kynurenine were among the metabolites upregulated in 2-year compared to 3-month mice, while glutamate and gamma aminobutyric acid (GABA) metabolites were decreased (SFigure 5). Previous research has found a similar result upon loss of *Opa-1,* which typically favors fatty acid synthesis [46–48].

DISCUSSION:

Heart failure may be intrinsically linked to mitochondria [4629] and understanding the aging of mitochondria and the role the MICOS complex plays in it is crucial. We demonstrated changes that occur in fibroblasts upon the loss of the MICOS complex. Additionally, we found that while some changes in mitochondria morphology occurs across aging, but, compared to prior studies, less fragmentation occurred.

Importantly, our study combined TEM and SBF-SEM, and was novel in using 3D reconstruction to look at aging cardiac muscle. TEM is an important technique for measuring cristae due to its very high x- and y- resolution [39]. However, it is limited in accurately measuring mitochondria, which are 3D objects that cannot be accurately represented in 2D. Therefore, also using SBF-SEM for 3D reconstruction can allow for a more complete understanding of the mitochondria morphology. Future studies may consider also utilizing focused ion beam-scanning electron microscopy, which allows for the 3D reconstruction of smaller objects such as cristae [49]. In the past, FIB-SEM has successfully been performed in mouse muscle to characterize mitochondria [50]. Additionally, mitochondria has been quantified through SBF-SEM in both human and mouse muscles in other studies, such as that by Vincent et al [36]. However, given that cardiac muscle is responsible for the proper contractile of the heart, there remains a gap in the literature in studying it, and our 3D reconstruction begins to elucidate how cardiac muscle changes across aging in a mouse model. This highlighted the importance of further exploring how changes in skeletal muscle specifically affect their form and function through the knockout of the MICOS complex, which we believe may be implicated in aging.

Across aging, we saw that the MICOS gene transcripts deteriorated (Figure 4). Additionally, we observed in 3D reconstructions that loss of *Opa-1, Mitofilin, Chchd3,* and *Chchd6* resulted in high mitochondrial dysfunction. This was marked by fragmentation, lamellar mitochondria, much smaller mitochondria, and reduced OCR (Figure 5). Therefore, it would be expected that since *Opa-1, Mitofilin, Chchd3,* and *Chchd6* are lost over time, their effects on the

mitochondria would be felt. However, when we examined the aged model, it was contrary to this in some ways.

It is understood that physical and physiological changes occur across age (Figure 1A-E; SFigure 1). However, in cardiac tissue, across aging, we observed that mitochondria number increased while the area decreased (Figure 1D-E). This suggests mitochondria fission is increasingly happening, and fusion is happening, mimicking the effects of OPA-1 loss or DRP-1 upregulation [5,17]. However, 3D reconstruction did not show as much fragmentation (Figure 2), with less network formation than the skeletal muscle (Figure 3). Critically, all of the skeletal muscle showed nanotunnels, which are mitochondrial structures which allow for transport of materials and greater mitochondria communication [35]. Although past studies have observed nanotunnels in disease states [35], we noticed no nanotunnels formed in cardiac muscle, even in aged samples. In cardiac muscle, the mitochondria underwent less fragmenting and less network formation and they did not form nanotunnels (Figure 2-3). We also found lesser complexity in the cardiac mitochondria (Figure 3) and observed that the mitochondria underwent fewer changes with age than we have previously seen in skeletal muscle. It is possible that heart and skeletal muscle respond to aging differently due to differences in nucleation. Skeletal muscles are typically multi-nucleated [11]. As such, even if mitochondria are fragmented, they can still function through the sharing of cellular components. In contrast, heart cells are mono-nucleated. As a result, it may be harder for heart to recover in the loss of mitochondrial efficiency. As such, more resources may be dedicated to ensuring that mitochondria maintain their form, and thus their function in cardiac muscle.

Mitochondria shape may be implicated in heart failure [29], which makes the specific study of cardiac muscle across aging an important therapeutic target. Previously, research has proposed the MFRTA, which speculates that reactive oxygen species alter functions of mitochondria, such as ATP production, to induce aging [12]. As a mechanism to avoid such a mechanism, it is possible the heart ensures more resources to ensuring that mitochondria do not entered stress states, potentially through mitochondria endoplasmic reticulum contacts (MERCs). Future research may consider analyzing MERCs in cardiac muscle to better see how signaling and exchange of calcium changes in stressed mitochondrial states of the heart.

Metabolomics analysis shows that pathways associated with steroidogenesis and fatty acid metabolism across aging (Figure 6). For example, fumarate upregulation in the 2-year sample suggests that the citric acid cycle, which is cardioprotective, is upregulated [51] (SFigure 5). Similarly, kynurenine, which is neuroprotective but also may play roles in energy production [52], are upregulated (Figure 6C). However, fatty acid metabolism is underscored across the metabolomic analysis. Furthermore, metabolites, such as malonate, associated with fatty acid metabolism are also upregulated across aging [53]. We hypothesize that a potential reason cardiac tissue mitochondria undergo less drastic morphological changes across aging is due to this increased metabolism. It is possible that the reduced energy production of mitochondria are supplemented with other forms of energy production. Furthermore, we observed more lipid droplets across aging (Figure 1M). These lipid droplets may be physically interacting with mitochondria [54] to maintain energy homeostasis across aging. Further analysis may consider better measuring and quantifying changes in lipid-mitochondria interactions and their effects on the functioning of the tissue.

In conclusion, here we combine TEM and 3D reconstructions to evaluate mitochondria and cristae morphology in male mouse cardiac muscle. Specifically, we found that cardiac muscle across aging differentially react compared to prior studies, while the MICOS complex

both decreases with age and loss of MICOS complex results in high mitochondrial dysfunction marked by changes in mitochondrial structure. This suggests a potential mechanism that protects cardiac muscle mitochondria from complete fragmentation and formation of nanotunnels in mitochondria. Future studies can explore this mechanism and continue to elucidate the link between age-related heart failure, the MICOS complex, and dysfunction in the mitochondria.

EXPERIMENTAL PROCEDURES

Animal Care and Maintenance

The University of Iowa Animal Care and Use Committee (IACUC) approved all the procedures that were used for care of mice. These protocols are previously described [15] and follow the National Institute of Health Guide for the Care and Use of Laboratory Animals recommendations. WT male C57Bl/6J mice were exclusively used in experiments. They were housed at 22°C on a 12-hour light, 12-hour dark cycle. They had free access to water and standard chow. 5% isoflurane/95% oxygen was used to anesthetize mice.

RNA Extraction and RT-qPCR

Using TRIzol reagent (Invitrogen), RNA was extracted from tissue. From there the RNeasy kit (Qiagen Inc) was used to purify it and it was subsequently quantitated by the absorbance at 260 nm and 280 nm using a NanoDrop 1000 (NanoDrop products, Wilmington, DE, USA) spectrophotometer. Isolated RNA (~1 µg), using a High-Capacity cDNA Reverse Transcription Kit (Applied Biosciences, Carlsbad CA), underwent reverse-transcription. From there, SYBR Green (Life Technologies, Carlsbad, CA) [1] were used to perform real-time quantitative PCR (qPCR). Three samples for each qPCR (~50 ng) were placed in a 384-well plate that was subsequently underwent qPCR in ABI Prism 7900HT instrument (Applied Biosystems). The specific cycle they underwent was: 1 cycle at 95°C for 10 min; 40 cycles of 95°C for 15 s; 59°C for 15 s, 72°C for 30 s, and 78°C for 10 s; 1 cycle of 95°C for 15 s; 1 cycle of 60°C for 15 s; and one cycle of 95°C for 15 s. Once results were normalized to glyceraldehyde-3-phosphate dehydrogenase (*GAPDH*), data is shown as fold changes. qPCR primers were previously published sequences [15] as shown in Table 1.

Table 1: qPCR Primers Used

Gene	Primers	
Opa-1	Forward	5’-ACCAGGAGACTGTGTCAA-3’
	Reverse	5’-TCTTCAAATAAACGCAGAGGTG-3’
CHCHD3	Forward	5’-GAAAAGAATCCAGGCCCTTCCACGCGC-3’
	Reverse	5’-CAGTGCCTAGCACTTGGCACAACCAGGAA-3’
CHCHD6	Forward	5’-CTCAGCATGGACCTGGTAGGCACTGGGC-3’
	Reverse	5’-GCCTCAATTCCCACATGGAGAAAGTGGC-3’
Mitofilin	Forward	5’-CCTCCGGCAGTGTTCACCTAGTAACCCCTT-3’
	Reverse	5’-TCGCCCGTCGACCTTCAGCACTGAAAACCTAT-3’

CRISPR-Cas9 Knockouts

Adenovirus was used to infect cardiomyocytes to produce the following knockouts—control CRISPR/Cas9 (sc-418922), *CHCHD6* (Mic25) CRISPR (sc-425817), *CHCHD3* (Mic19) CRISPR (sc-425804), and *mitofilin* (Mic60) CRISPR (sc-429376) (Santa Cruz Biotechnology, California, US), with the use of guide RNA (Table 2). For each of the CRISPR 2.5% was combined with 2.5% RNAiMax (ThermoFisher Scientific; 13778075) and the remaning solution was Opti-MEM (Gibco; 31985070) and they were incubated at room temperature for 20 minutes. The media was removed from the cells, and after washing twice with PBS, 200 µL of the CRISPR mixture and 800 µl of Opti-MEM was added to each sample, and they were incubated at 37 C for 4 hours. An additional 1 mL of DMEM medium was added before cells were incubated at 37 C overnight. Cardiocytes were then washed with PBS, and fresh medium was added. After 3 and 7 days, following infection, experiments were performed.

Table 2: Guide RNA and Plasmids Used

Gene Name	Type of Plasmid	CAS Number
Mitofilin	CRISPR/Cas9 KO (m)	sc-429376
CHCHD6	CRISPR/Cas9 KO (m)	sc-425817
CHCHD3	CRISPR/Cas9 KO (m)	sc-425804
Control	CRISPR/Cas9 KO (m)	sc-418922

Serial Block-Face Scanning Electron Microscope (SBF-SEM) Processing of Mouse Muscle Fibers

SBF-SEM was performed as described previously [16,49,55]. 5% isoflurane was used to anesthetize male mice. Once the hair and skin were removed, the hindlimbs were incubated in 2% glutaraldehyde with 100 mM phosphate buffer for 30 min. Gastrocnemius muscles were dissected, cut into 1-mm^3 cubes, and incubated in 2.5% glutaraldehyde, 1% paraformaldehyde, 120 mM sodium cacodylate solution for 1 hour.

From there, 100 mM cacodylate buffer at room temperature was used to wash tissue three times. Tissue was then immersed in 3% potassium ferrocyanide and 2% osmium tetroxide for 1 hour at 4°C. After this, they were washed with deionized water three times and transferred to 0.1% thiocarbohydrazide and 2% filtered osmium tetroxide and they were incubated for 30 min. Finally, they were again washed with deionized water three times and transferred to 1% uranyl acetate and left overnight at 4°C. The next day, they were washed and samples were transferred to an 0.6% lead aspartate solution for 30 min at 60°C. From there, dehydration was performed by a gradient of five min each in progressively going up, 20%, 50%, 70%, 90%, 95%, and 100% acetone. Cardiac tissues were impregnated in Epoxy Taab 812 hard resin, then moved to new resin, and polymerization occurred at 60°C for 36–48 hours. Blocks of resin were sectioned, cut to 0.5 mm × 0.5 mm, and glued to aluminum pins. These pins were transferred to the FEI/Thermo Scientific Volumescope 2 SEM. 300−400 ultrathin (0.09 µm) serial sections from each of the blocks were collected for conventional TEM. All sections were collected onto formvar-coated slot grids (Pella, Redding CA), stained, and imaged as previously described [16,49,55].

Measurement of OCR Using Seahorse

Using an XF24 bioanalyzer (Seahorse Bioscience: North Billerica, MA, USA), oxygen consumption rate was measured for *OPA1*, *CHCHD3*, *CHCHD6*, or *Mitofilin* KD fibroblasts as previously described[15].

Quantification of TEM Micrographs and Parameters Using ImageJ
The National Institutes of Health (NIH) *ImageJ* software was used for quantification of TEM images, as described previously [39,49]. Each cell of interest was divided into four equal quadrants and half of these quadrants were randomly selected. From those randomly selected, 3 blind individuals measured and quantified them. A minimum of 10 cells were measured by each individual and their findings were then averaged. To verify with accurate and reproducible values, the number of cells analyzed by each individual was increased to 30 if there was high variability.

Segmentation and Quantification of 3D SBF-SEM Images Using Amira
SBF-SEM images were manually segmented in Amira to perform 3D reconstruction, as described previously [16,49]. For each 3D reconstruction, (300−400 slices) were obtained and these were transferred onto Amira. By hand by an individual blind to which samples came from which, structural features were traced manually on sequential slices of micrograph blocks. For each of the 3D reconstructions of cardiac muscle in mice, 30-50 serial sections were chosen at approximately equal z-direction intervals, stacked, aligned, and visualized using Amira to make videos and quantify volumetric structures. 500 total mitochondria across from 3 mice were collected for each quantification. For 3D reconstruction of cardiomyocytes, a minimum of 10 cells were chosen and from them approximately 20 mitochondria from each cell were segmented for a total of about 200 mitochondria. Quantification of 3D structures was performed as described previously [16] using the Amira software (Thermo Scientific). Many parameters were automatically measured by Amira. Algorithms for measurements were entered manually for those not already in the system.

Data Analysis
All SBF-SEM and TEM data were performed in at least three independent experiments and are presented as the mean across these experiments. In presentation, black bars represent the standard error, and dots represent individual data points shown. For data with only two groups, an unpaired, t-test was used. If more than two groups were compared, one-way ANOVA was performed, and significance was assessed using Fisher's protected least significant difference (LSD) test. For both of these analyses, GraphPad Prism software package was used (La Jolla, CA, USA). A minimum threshold of $p < 0.05$ indicated a significant difference. Higher degrees of statistical significance (**, ***, ****) were defined as $p < 0.01$, $p < 0.001$, and $p < 0.0001$, respectively.

ACKNOWLEDGEMENTS
We would like to thank Mariya Sweetwyne for her advice as an aging expert.

FUNDING
This work was supported by UNCF/BMS EE United Negro College Fund/Bristol-Myers Squibb E.E. T-32, number DK007563 entitled Multidisciplinary Training in Molecular Endocrinology to Z.V.; Just Postgraduate Fellowship in the Life Sciences Fellowship to H.K.B.; NSF MCB

#2011577I to S.A.M.; The United Negro College Fund/Bristol-Myers Squibb E.E. Just Faculty Fund, Burroughs Wellcome Fund Career Awards at the Scientific Interface Award, Burroughs Wellcome Fund Ad-hoc Award, National Institutes of Health Small Research Pilot Subaward to 5R25HL106365-12 from the National Institutes of Health PRIDE Program, DK020593, Vanderbilt Diabetes and Research Training Center for DRTC Alzheimer's Disease Pilot & Feasibility Program to A.H.J. Its contents are solely the responsibility of the authors and do not necessarily represent the official view of the NIH. The funders had no role in study design, data collection and analysis, decision to publish, or preparation of the manuscript.

CONFLICT OF INTEREST

The authors declare that they have no conflict of interest.

References:

1. Boudina, S. *et al.* Mitochondrial energetics in the heart in obesity-related diabetes: direct evidence for increased uncoupled respiration and activation of uncoupling proteins. *Diabetes* **56**, 2457–2466 (2007).
2. Brown, D. A. *et al.* Mitochondrial function as a therapeutic target in heart failure. *Nat Rev Cardiol* **14**, 238–250 (2017).
3. Tyumentsev, M. A., Stefanova, N. A., Kiseleva, E. V. & Kolosova, N. G. Mitochondria with Morphology Characteristic for Alzheimer's Disease Patients Are Found in the Brain of OXYS Rats. *Biochemistry Moscow* **83**, 1083–1088 (2018).
4. Alaimo, A. *et al.* Deregulation of Mitochondria-Shaping Proteins Opa-1 and Drp-1 in Manganese-Induced Apoptosis. *PLOS ONE* **9**, e91848 (2014).
5. Lee, Y., Jeong, S.-Y., Karbowski, M., Smith, C. L. & Youle, R. J. Roles of the mammalian mitochondrial fission and fusion mediators Fis1, Drp1, and Opa1 in apoptosis. *Molecular biology of the cell* **15**, 5001–5011 (2004).
6. Zuo, W. *et al.* Mitochondria autophagy is induced after hypoxic/ischemic stress in a Drp1 dependent manner: the role of inhibition of Drp1 in ischemic brain damage. *Neuropharmacology* **86**, 103–115 (2014).

7. Gunter, T. E., Yule, D. I., Gunter, K. K., Eliseev, R. A. & Salter, J. D. Calcium and mitochondria. *FEBS letters* **567**, 96–102 (2004).
8. Mehta, M. M., Weinberg, S. E. & Chandel, N. S. Mitochondrial control of immunity: beyond ATP. *Nat Rev Immunol* **17**, 608–620 (2017).
9. Nicholls, D. G. Mitochondria and calcium signaling. *Cell calcium* **38**, 311–317 (2005).
10. Barja, G. The mitochondrial free radical theory of aging. *Progress in molecular biology and translational science* **127**, 1–27 (2014).
11. Figueiredo, P. A., Mota, M. P., Appell, H. J. & Duarte, J. A. The role of mitochondria in aging of skeletal muscle. *Biogerontology* **9**, 67–84 (2008).
12. Sanz, A. & Stefanatos, R. K. The mitochondrial free radical theory of aging: a critical view. *Current aging science* **1**, 10–21 (2008).
13. Cipolat, S., de Brito, O. M., Dal Zilio, B. & Scorrano, L. OPA1 requires mitofusin 1 to promote mitochondrial fusion. *Proceedings of the National Academy of Sciences* **101**, 15927–15932 (2004).
14. Otera, H., Miyata, N., Kuge, O. & Mihara, K. Drp1-dependent mitochondrial fission via MiD49/51 is essential for apoptotic cristae remodeling. *Journal of Cell Biology* **212**, 531–544 (2016).
15. Pereira, R. O. *et al*. OPA 1 deficiency promotes secretion of FGF 21 from muscle that prevents obesity and insulin resistance. *The EMBO journal* **36**, 2126–2145 (2017).
16. Garza-Lopez, E. *et al.* Protocols for Generating Surfaces and Measuring 3D Organelle Morphology Using Amira. *Cells* **11**, 65 (2022).
17. Frezza, C. *et al.* OPA1 controls apoptotic cristae remodeling independently from mitochondrial fusion. *Cell* **126**, 177–189 (2006).

18. Cogliati, S., Enriquez, J. A. & Scorrano, L. Mitochondrial cristae: where beauty meets functionality. *Trends in biochemical sciences* **41**, 261–273 (2016).
19. Harner, M. E. *et al.* An evidence based hypothesis on the existence of two pathways of mitochondrial crista formation. *eLife* **5**, e18853 (2016).
20. Stephan, T. *et al.* MICOS assembly controls mitochondrial inner membrane remodeling and crista junction redistribution to mediate cristae formation. *The EMBO journal* **39**, e104105 (2020).
21. Mannella, C. A. Consequences of folding the mitochondrial inner membrane. *Frontiers in Physiology* **11**, 536 (2020).
22. Glytsou, C. *et al.* Optic atrophy 1 is epistatic to the core MICOS component MIC60 in mitochondrial cristae shape control. *Cell reports* **17**, 3024–3034 (2016).
23. Eramo, M. J., Lisnyak, V., Formosa, L. E. & Ryan, M. T. The 'mitochondrial contact site and cristae organising system' (MICOS) in health and human disease. *The Journal of Biochemistry* **167**, 243–255 (2020).
24. Kozjak-Pavlovic, V. The MICOS complex of human mitochondria. *Cell and tissue research* **367**, 83–93 (2017).
25. Kondadi, A. K. *et al.* Cristae undergo continuous cycles of membrane remodelling in a MICOS-dependent manner. *EMBO reports* **21**, e49776 (2020).
26. Friedman, J. R., Mourier, A., Yamada, J., McCaffery, J. M. & Nunnari, J. MICOS coordinates with respiratory complexes and lipids to establish mitochondrial inner membrane architecture. *Elife* **4**, e07739 (2015).
27. Zhang, J. *et al.* Alterations in mitochondrial dynamics with age-related Sirtuin1/Sirtuin3 deficiency impair cardiomyocyte contractility. *Aging Cell* **20**, e13419 (2021).

28. Parra, V. *et al.* Insulin stimulates mitochondrial fusion and function in cardiomyocytes via the Akt-mTOR-NFκB-Opa-1 signaling pathway. *Diabetes* **63**, 75–88 (2014).

29. Kenny, H. C. & Abel, E. D. Heart Failure in Type 2 Diabetes Mellitus. *Circ Res* **124**, 121–141 (2019).

30. Kim, J., Wei, Y. & Sowers, J. R. Role of mitochondrial dysfunction in insulin resistance. *Circulation research* **102**, 401–414 (2008).

31. Friederich, M., Hansell, P. & Palm, F. Diabetes, oxidative stress, nitric oxide and mitochondria function. *Current diabetes reviews* **5**, 120–144 (2009).

32. Ngoh, G. A., Papanicolaou, K. N. & Walsh, K. Loss of mitofusin 2 promotes endoplasmic reticulum stress. *Journal of Biological Chemistry* **287**, 20321–20332 (2012).

33. Glancy, B., Kim, Y., Katti, P. & Willingham, T. B. The Functional Impact of Mitochondrial Structure Across Subcellular Scales. *Front Physiol* **11**, 541040 (2020).

34. Willingham, T. B., Ajayi, P. T. & Glancy, B. Subcellular Specialization of Mitochondrial Form and Function in Skeletal Muscle Cells. *Front Cell Dev Biol* **9**, 757305 (2021).

35. Vincent, A. E., Turnbull, D. M., Eisner, V., Hajnóczky, G. & Picard, M. Mitochondrial Nanotunnels. *Trends Cell Biol* **27**, 787–799 (2017).

36. Vincent, A. E. *et al.* Quantitative 3D mapping of the human skeletal muscle mitochondrial network. *Cell reports* **26**, 996–1009 (2019).

37. Lesnefsky, E. J., Chen, Q. & Hoppel, C. L. Mitochondrial Metabolism in Aging Heart. *Circ Res* **118**, 1593–1611 (2016).

38. Chaudhary, K. R., El-Sikhry, H. & Seubert, J. M. Mitochondria and the aging heart. *J Geriatr Cardiol* **8**, 159–167 (2011).

39. Lam, J. *et al.* A Universal Approach to Analyzing Transmission Electron Microscopy with ImageJ. *bioRxiv* (2021).

40. Eisner, V., Picard, M. & Hajnóczky, G. Mitochondrial dynamics in adaptive and maladaptive cellular stress responses. *Nat Cell Biol* **20**, 755–765 (2018).

41. Mallay, S., Gill, R., Young, A. & Mailloux, R. J. Sex-dependent Differences in the Bioenergetics of Liver and Muscle Mitochondria from Mice Containing a Deletion for glutaredoxin-2. *Antioxidants (Basel)* **8**, E245 (2019).

42. Lee, S.-J., Zhang, J., Choi, A. M. K. & Kim, H. P. Mitochondrial dysfunction induces formation of lipid droplets as a generalized response to stress. *Oxid Med Cell Longev* **2013**, 327167 (2013).

43. Vendelin, M. *et al*. Mitochondrial regular arrangement in muscle cells: a “crystal-like” pattern. *American Journal of Physiology-Cell Physiology* **288**, C757–C767 (2005).

44. Tezze, C. *et al.* Age-Associated Loss of OPA1 in Muscle Impacts Muscle Mass, Metabolic Homeostasis, Systemic Inflammation, and Epithelial Senescence. *Cell Metab* **25**, 1374-1389.e6 (2017).

45. Arevalo, J. A., Miller, M. L., Vazquez-Medina, J. P. & Brooks, G. A. Mitochondrial Fragmentation in Skeletal Muscle Derived Cells from an Old Male Donor May Relate to Decreased Oxygen Consumption Rates. *The FASEB Journal* **34**, 1–1 (2020).

46. Wasilewski, M. *et al.* Optic Atrophy 1-Dependent Mitochondrial Remodeling Controls Steroidogenesis in Trophoblasts. *Current Biology* **22**, 1228–1234 (2012).

47. Sarzi, E. *et al.* Increased steroidogenesis promotes early-onset and severe vision loss in females with OPA1 dominant optic atrophy. *Human Molecular Genetics* **25**, 2539–2551 (2016).

48. Chao de la Barca, J. M. *et al*. Metabolomics hallmarks OPA1 variants correlating with their in vitro phenotype and predicting clinical severity. *Hum Mol Genet* **29**, 1319–1329 (2020).

49. Hinton, A. *et al.* A comprehensive approach for artifact-free sample preparation and assessment of mitochondrial morphology in tissue and cultured cells. *bioRxiv* (2021).

50. Glancy, B. *et al.* Mitochondrial reticulum for cellular energy distribution in muscle. *Nature* **523**, 617–620 (2015).

51. Ashrafian, H. *et al.* Fumarate Is Cardioprotective via Activation of the Nrf2 Antioxidant Pathway. *Cell Metabolism* **15**, 361–371 (2012).

52. Savitz, J. The kynurenine pathway: a finger in every pie. *Mol Psychiatry* **25**, 131–147 (2020).

53. Li, S., Fu, W., Su, R., Zhao, Y. & Deng, Y. Metabolic engineering of the malonyl-CoA pathway to efficiently produce malonate in Saccharomyces cerevisiae. *Metabolic Engineering* **73**, 1–10 (2022).

54. Pu, J. *et al.* Interactomic study on interaction between lipid droplets and mitochondria. *Protein Cell* **2**, 487–496 (2011).

55. Neikirk, K. *et al.* Systematic Transmission Electron Microscopy-Based Identification of Cellular Degradation Machinery. *bioRxiv* (2021).

Figure Legend:

Figure 1: Changes in cardiac muscle mitochondria and cristae across aging revealed in TEM and heart data.
Changes in (**A**) body weight, (**B**) amount of lean mass, (**C**) amount of fat mass, and the mass of hearts (**D**) change in mice across their aging. Each dot represents a mouse sampled. (**E**) Furthermore, glucose tolerance test shows there is altered glucose tolerance. Representative transmission electron micrographs for cardiac muscle at (**F**) 3-months, (**F'**) 1-year (**F''**) and 2-years in male mouse skeletal muscle. Quantification of key mitochondria characteristics included (**G**) the number of mitochondria normalized to the area surveyed, (**H**) average

mitochondria area, and (**I**) circularity index, which is measures mitochondrial shape. For cristae, (**J**) the amount of cristae (**K**) and cristae score, a measurement of the quality of cristae observed, are shown. Each dot represents a mitochondria. Representative image of lipids stained with Oil Red O in cardiac muscle at (**L**) 3-months and (**L'**) 2-years. Quantification of key lipid characteristics, (**M**) lipid number, normalized to area surveyed, and (**N**) average lipid droplet area. Significance values *, **, ***, **** indicate $p \leq 0.05$, $p \leq 0.01$, $p \leq 0.001$, and $p \leq 0.0001$, respectively.

Figure 2: Changes in cardiac muscle mitochondria morphology across aging revealed in SBF-SEM. (**A-C**) Representative SBF-SEM orthoslice for cardiac muscle. (**A'-C'**) 3D reconstructions of mitochondria in male cardiac tissues of different ages overlaid on ortho slices. (**A''-C''**) 3D reconstructed and isolated mitochondria for clear visualization. (**D-F**) 3D reconstructions were then quantified. (**D**) Mitochondrial volume in cardiac muscle of different ages. (**E**) 3D area of the average mitochondria in cardiac muscle. (**F**) Perimeter of the average mitochondria in cardiac muscle. Each dot represents the average of a single mouse. Significance values *, **, ***, **** indicate $p \leq 0.05$, $p \leq 0.01$, $p \leq 0.001$, and $p \leq 0.0001$, respectively.

Figure 3: Changes in cardiac muscle branching and networking across aging revealed in TEM. (**A-C**) 3D reconstruction of individually colored mitochondria from a transverse view for mouse cardiac muscle of different ages. (**A'-C'**) 3D reconstruction of individually colored mitochondria from a longitudinal view in cardiac muscle tissues of different ages. (**D**) Mitochondria 3D reconstructions were further organized by volume for each of the age cohorts. (**E**) To measure shape, sphericity changes across aging in cardiac muscle was further measured. (**F**) To measure complexity, mitochondria branching index was measured to estimate networking of mitochondria. Significance value **** and ** indicates $p \leq 0.0001$ and $p \leq 0.01$.

Figure 4: Transcription of *Opa-1* and MICOS genes in aging cardiac muscle.
(A-D) qPCR analyzing the gene transcript fold changes of Opa-1 and MICOS in cardiocytes across aging. (**A**) *Opa-1* transcripts. (**B**) *Mitofilin* transcripts. (**C**) *CHCHD3* transcripts. (**D**) *CHCHD6* transcripts. Significance values *, **, ***, **** indicate $p \leq 0.05$, $p \leq 0.01$, $p \leq 0.001$, and $p \leq 0.0001$, respectively.

Figure 5: Loss of *Opa-1* and MICOS genes result in mitochondrial structure changes and oxygen consumption rate changes. **(A)** Confocal fluorescence (using Mitotracker red) shows changes upon individual knockout (KO) of *Opa-1, Mitofilin, Chchd3,* and *Chchd6* in mouse cardiac muscle. Below this, individual KO of *Opa-1, Mitofilin, Chchd3,* and *Chchd6* was also observed in 3D reconstruction of SBF-SEM. (**B-D**) Quantification upon KO-state of each MICOS gene and *Opa-1* was performed in 3D reconstruction. (**B**) Mitochondria length and (**C)** mitochondria volume across each knockout. (**D**) Additionally, the relative frequency of mitochondria that presented as fragmented or tubular mitochondria was altered across knock outs. (**E**) Seahorse Analyzer was utilized to measure oxygen consumption rate (OCR) in *OPA1* and *mitofilin* KD. (**F**) Basal OCR, which shows only mitochondrial respiration, (**G**) ATP-linked, which was measured by ATP-inhibitor oligomycin, (**H**) maximum OCR, which represents maximum respiration, and (**I**) reserve capacity, signifies the extra amount extra ATP which can quickly be generated. (**J**) Oxygen consumption was also evaluated for *CHCHD3* and *CHCHD6*

KD, as well as their respective (**K**) basal OCR, (**L**) ATP-linked OCR, (**M**) maximum OCR, and (**N**) reserve capacity OCR.

Figure 6: Metabolomic Comparison across Age. (**A**) Metabolite *PCA and* (**B**) T-test comparing 3-month and 2-year mice (**C**) Heatmap showing the relative abundance of ions in 3-month versus 2-year mice. (**D**) Enrichment analysis metabolite showed enriched metabolites in 2-year mice.

Supplementary Figure 1. Echocardiographic parameters of male mouse at aged intervals of 3-month, 1-year, and 2-years. Presented as Means±SD. Key: HR indicates heart rate; EF, ejection fraction; CO, cardiac output; SV, stroke volume; LVT, left ventricle thickness; EAS, endoarea systolic; EAD, endoarea diastolic; EMS, endomajor systolic; EMD, endomajor diastolic; ESV, end systolic volume; EDV, end diastolic volume;

Supplementary Figure 2. Representative transmission electron micrographs for cardiac muscle at (**A**) 3-months, (**A'**) 1-year (**A''**) and 2-years in female mouse skeletal muscle. Quantification of key mitochondria characteristics were the same as male and included (**B**) the number of mitochondria normalized to the area surveyed, (**C**) average mitochondria area, and (**D**) circularity index, which is measures mitochondrial shape. For cristae, (**E**) the amount of cristae (**F**) and cristae score, a measurement of the quality of cristae observed, are shown. Significance values *, **, ***, **** indicate $p \leq 0.05$, $p \leq 0.01$, $p \leq 0.001$, and $p \leq 0.0001$, respectively.

Supplementary Figure 3. Individual quantifications for (**A**) average volume per mitochondria, (**B**) average 3D area of mitochondria, and (**C**) average perimeter of the mitochondria for each of the three mice sampled at 3-months, 1-year, and 2-years. For some graphs, outlying dots were removed for presentation, but all mitochondria values were considered in statistical analysis.

Supplementary Figure 4. (**A**) For each of the three male mice which were sampled at each aging time point, the mitochondrial branching index is shown. (**B**) The average sphericity values from each of the approximately 75 mitochondria surveyed per mice is also shown. For some graphs, outlying dots were removed for presentation, but all mitochondria values were considered in statistical analysis.

Supplementary Figure 5. Volcano plot of identified metabolites that were differentially regulated in 2-year samples compared to 3-month samples.

Video 1 – Confocal imaging of wildtype fibroblasts.
Video 2 – Confocal imaging of *OPA1* KD fibroblasts.
Video 3 – Confocal imaging of *Chchd3* KD fibroblasts.
Video 4 – Confocal imaging of *Mitofilin* KD fibroblasts

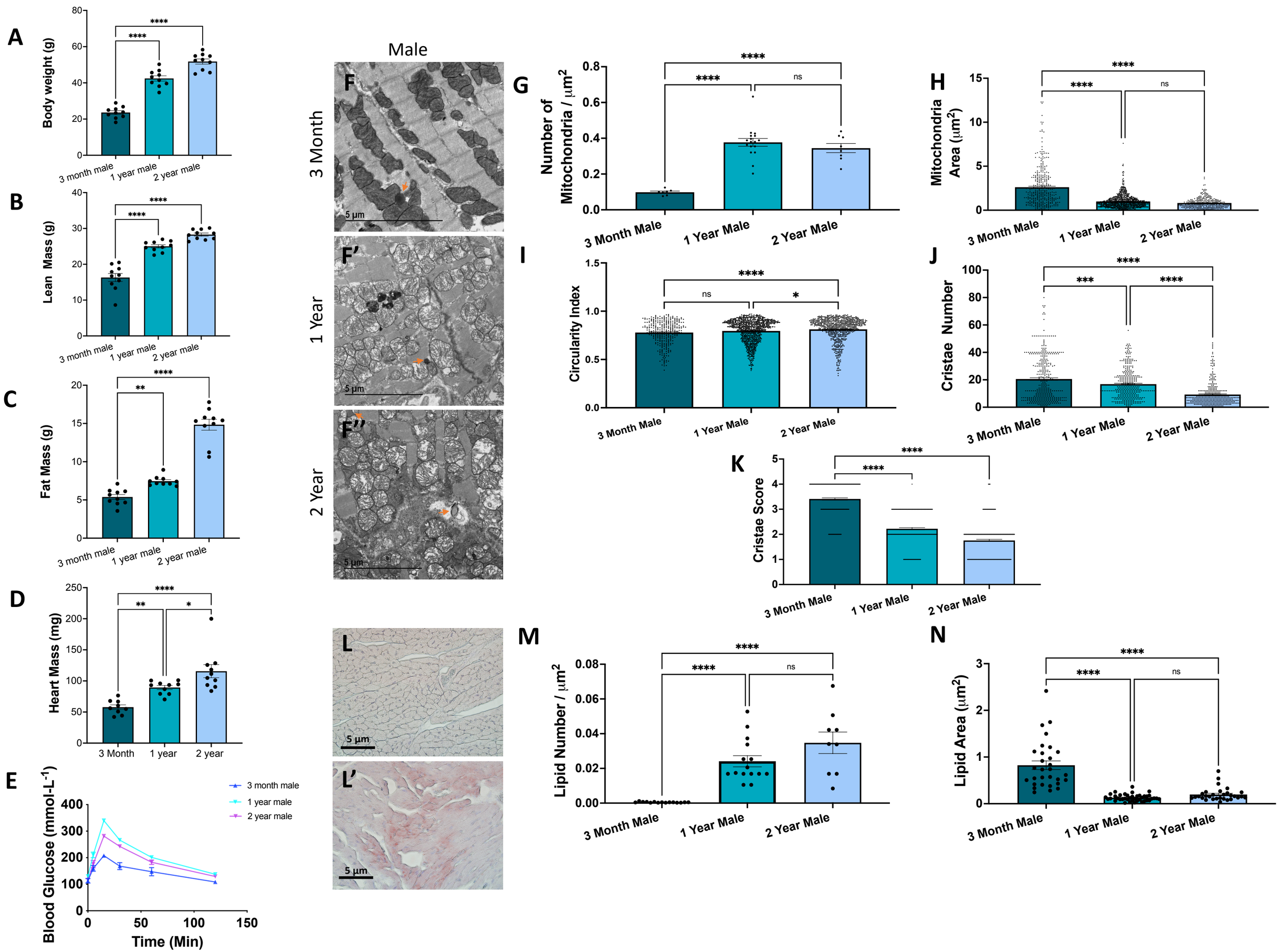
A
Body weight (g)
3 month male
1 year male
2 year male
B
Lean Mass (g)
C
Fat Mass (g)
D
Heart Mass (mg)
3 Month
1 year
2 year
E
Blood Glucose (mmol-L-1)
Time (Min)
Male
3 Month
1 Year
2 Year
F
F'
F''
5 µm
G
Number of Mitochondria / µm2
3 Month Male
1 Year Male
2 Year Male
H
Mitochondria Area (µm2)
I
Circularity Index
J
Cristae Number
K
Cristae Score
L
L'
M
Lipid Number / µm2
N
Lipid Area (µm2)
ns

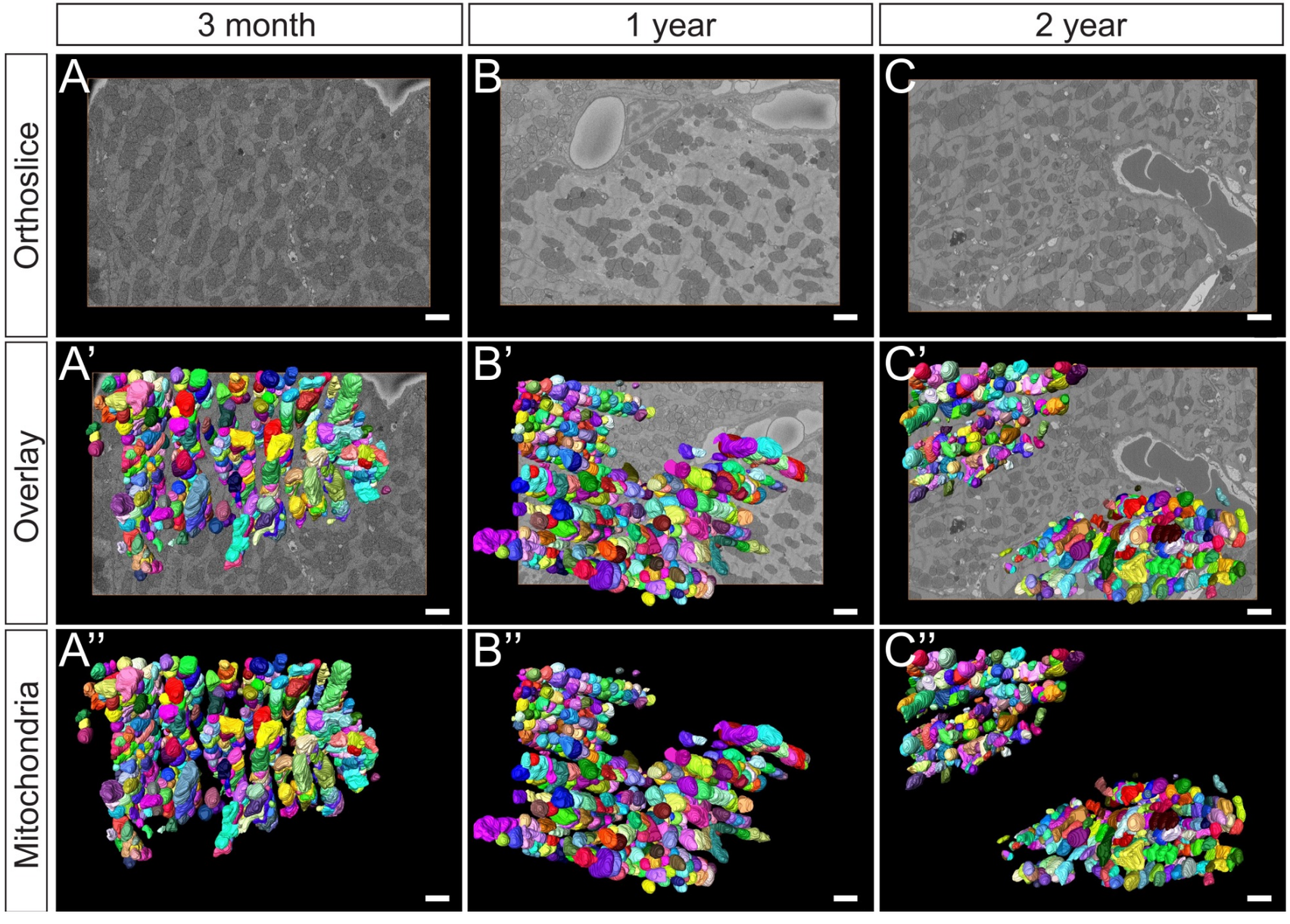
3 month
1 year
2 year
Orthoslice
Overlay
Mitochondria
A
B
C
A'
B'
C'
A''
B''
C''

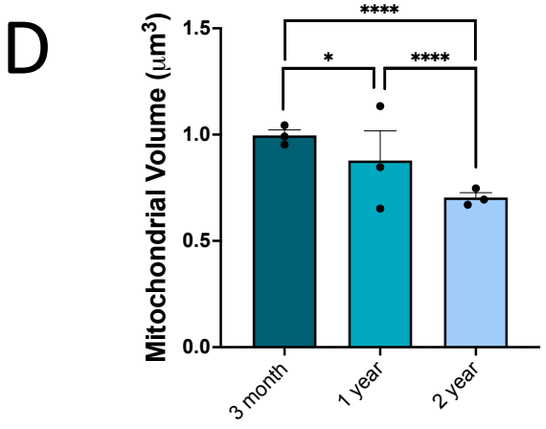
D
Mitochondrial Volume (μm³)
1.5
1.0
0.5
0.0
****
*
****
3 month
1 year
2 year

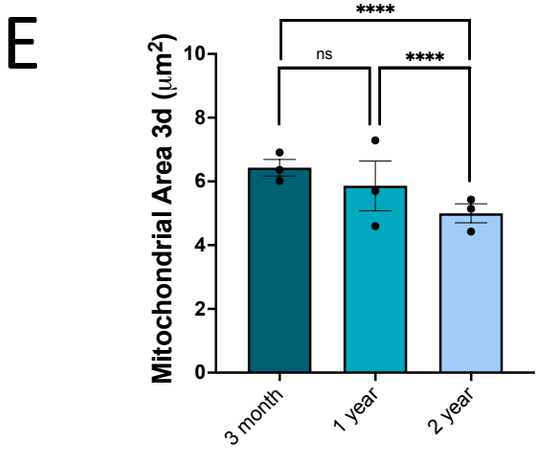
E
Mitochondrial Area 3d (μm²)
10
8
6
4
2
0
****
ns
****
3 month
1 year
2 year

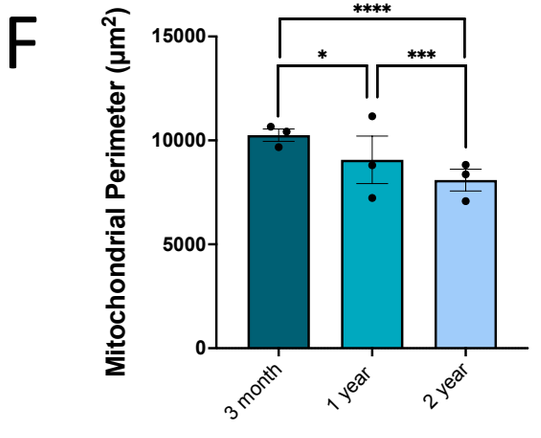
F
Mitochondrial Perimeter (μm²)
15000
10000
5000
0
****
*
***
3 month
1 year
2 year

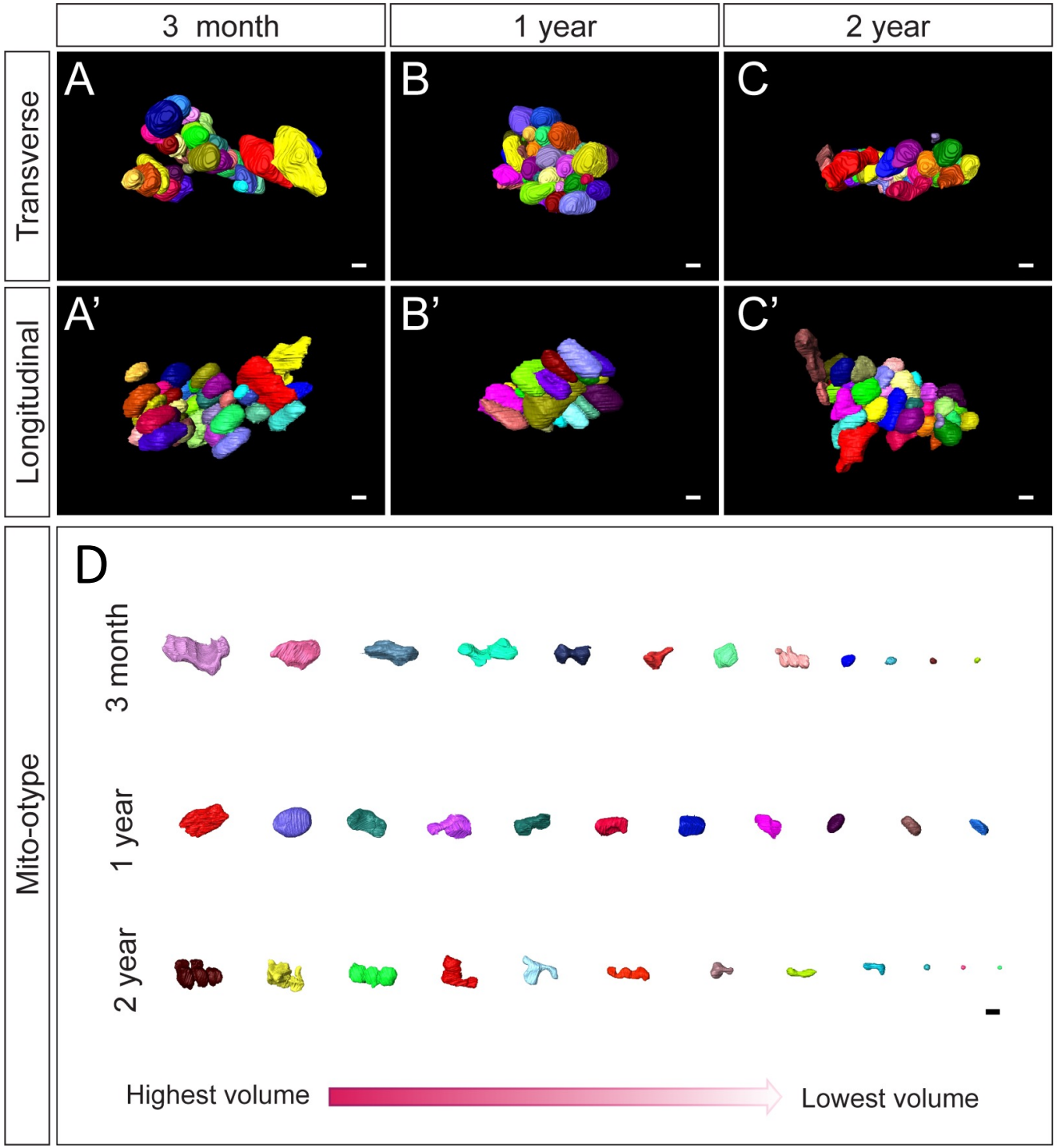
3 month
1 year
2 year
Transverse
Longitudinal
Mito-otype
A
B
C
A'
B'
C'
D
3 month
1 year
2 year
Highest volume
Lowest volume

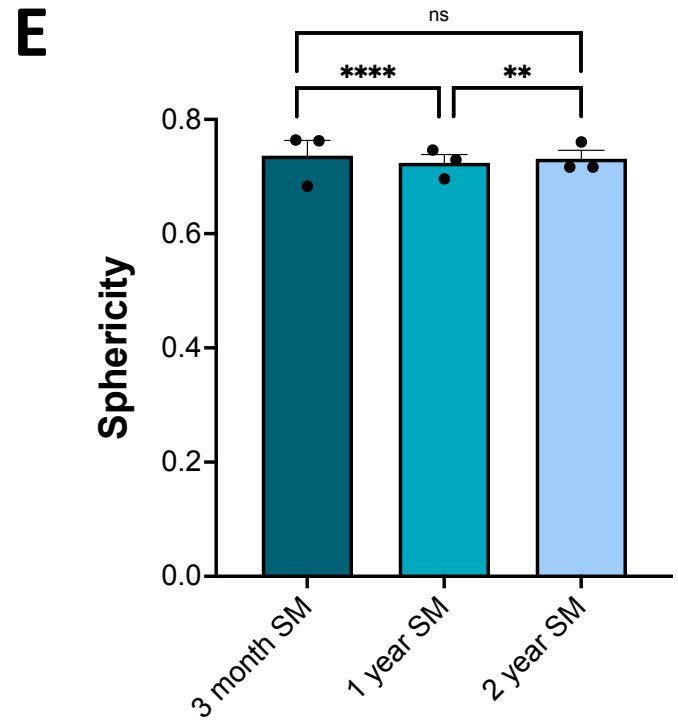
E
ns
****
**
Sphericity
0.8
0.6
0.4
0.2
0.0
3 month SM
1 year SM
2 year SM

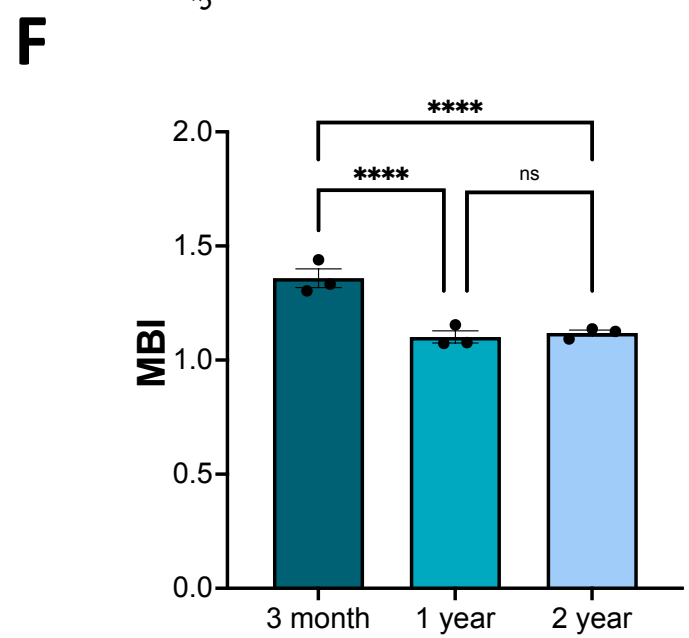
F
****
****
ns
MBI
2.0
1.5
1.0
0.5
0.0
3 month
1 year
2 year

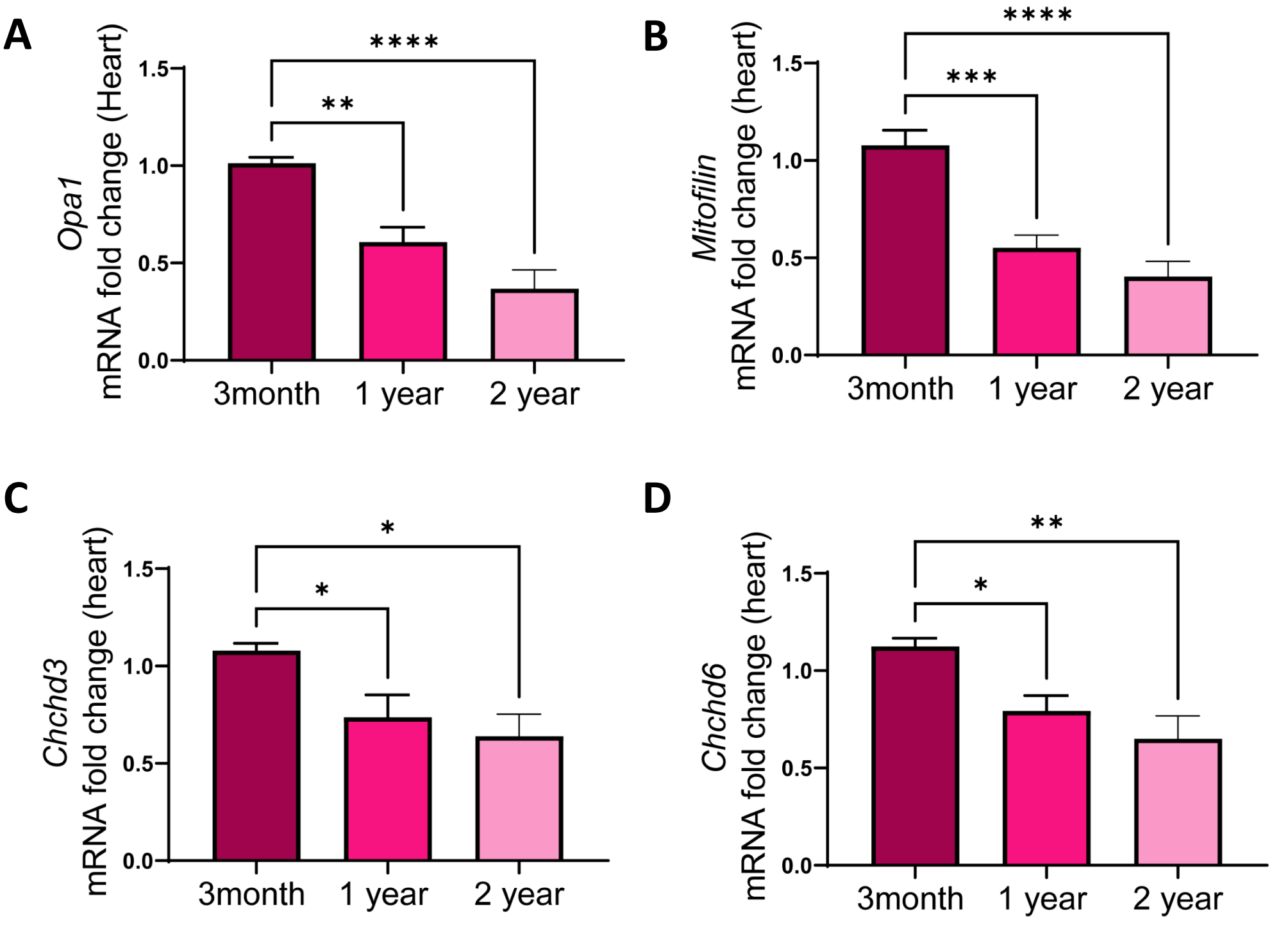
A
Opa1
mRNA fold change (Heart)
1.5
1.0
0.5
0.0
****
**
3month
1 year
2 year
B
Mitofilin
mRNA fold change (heart)
1.5
1.0
0.5
0.0
****
***
3month
1 year
2 year
C
Chchd3
mRNA fold change (heart)
1.5
1.0
0.5
0.0
*
*
3month
1 year
2 year
D
Chchd6
mRNA fold change (heart)
1.5
1.0
0.5
0.0
**
*
3month
1 year
2 year

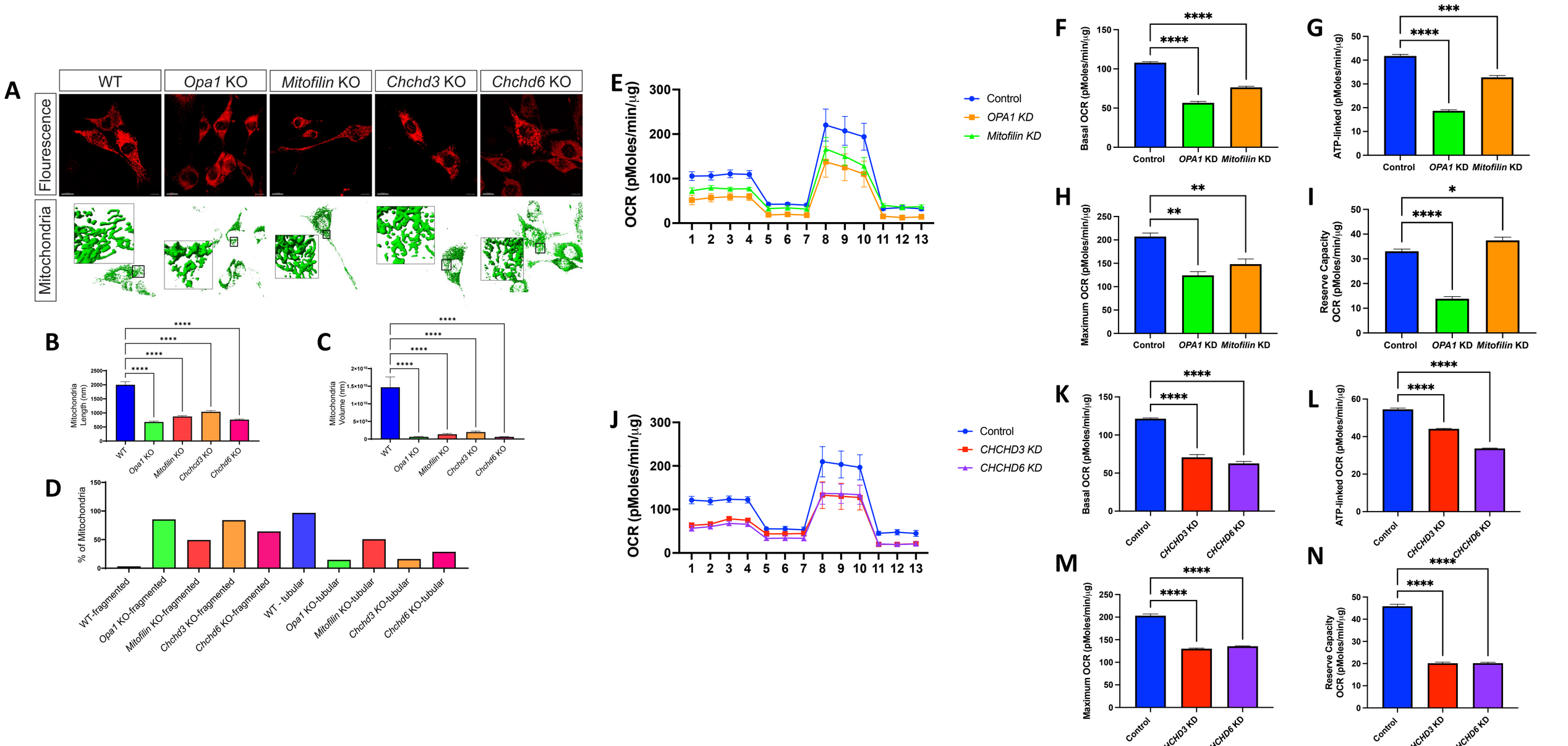
A
WT
Opa1 KO
Mitofilin KO
Chchd3 KO
Chchd6 KO
Flourescence
Mitochondria
B
Mitochondria Length (nm)
C
Mitochondria Volume (nm)
D
% of Mitochondria
WT-fragmented
Opa1 KO-fragmented
Mitofilin KO-fragmented
Chchd3 KO-fragmented
Chchd6 KO-fragmented
WT - tubular
Opa1 KO-tubular
Mitofilin KO-tubular
Chchd3 KO-tubular
Chchd6 KO-tubular
E
OCR (pMoles/min/µg)
Control
OPA1 KD
Mitofilin KD
F
Basal OCR (pMoles/min/µg)
G
ATP-linked (pMoles/min/µg)
H
Maximum OCR (pMoles/min/µg)
I
Reserve Capacity OCR (pMoles/min/µg)
J
OCR (pMoles/min/µg)
Control
CHCHD3 KD
CHCHD6 KD
K
Basal OCR (pMoles/min/µg)
L
ATP-linked OCR (pMoles/min/µg)
M
Maximum OCR (pMoles/min/µg)
N
Reserve Capacity OCR (pMoles/min/µg)

A

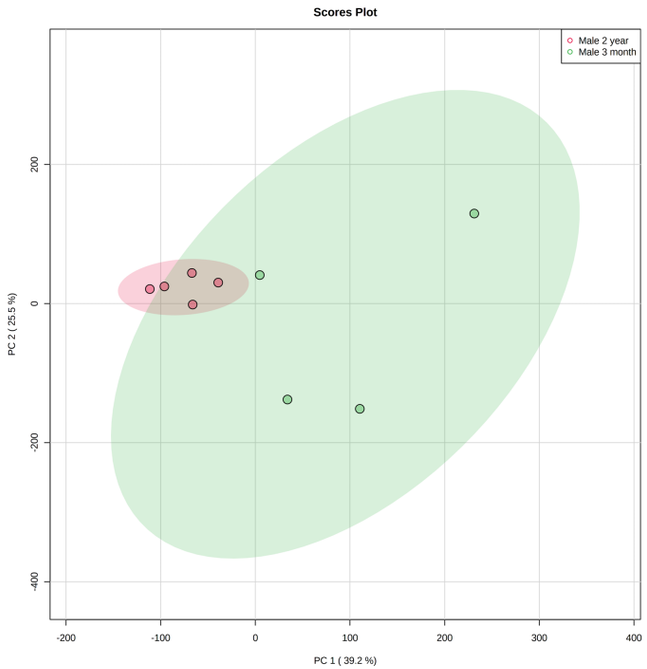
Scores Plot
Male 2 year
Male 3 month
PC 2 (25.5 %)
PC 1 (39.2 %)
200
0
-200
-400
-200
-100
0
100
200
300
400

B

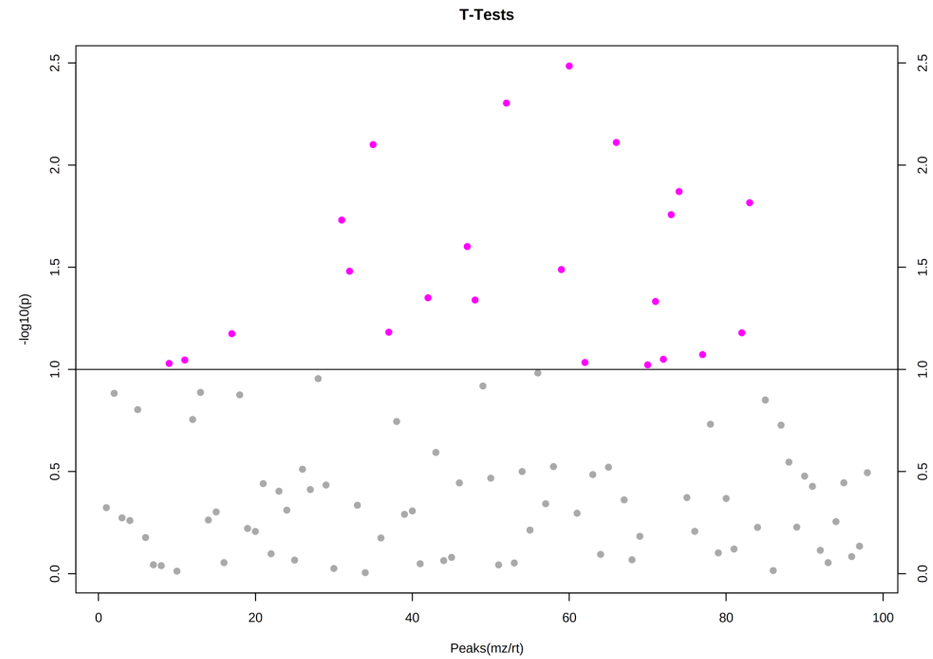
T-Tests
-log10(p)
Peaks(mz/rt)
0.0
0.5
1.0
1.5
2.0
2.5
0
20
40
60
80
100

C

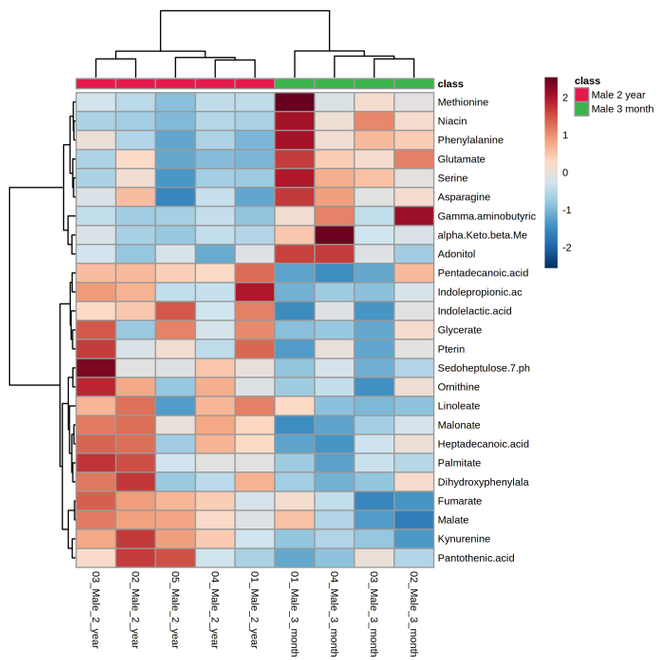
class
Male 2 year
Male 3 month
Methionine
Niacin
Phenylalanine
Glutamate
Serine
Asparagine
Gamma.aminobutyric
alpha.Keto.beta.Me
Adonitol
Pentadecanoic.acid
Indolepropionic.ac
Indolelactic.acid
Glycerate
Pterin
Sedoheptulose.7.ph
Ornithine
Linoleate
Malonate
Heptadecanoic.acid
Palmitate
Dihydroxyphenylala
Fumarate
Malate
Kynurenine
Pantothenic.acid
03_Male_2_year
02_Male_2_year
05_Male_2_year
04_Male_2_year
01_Male_2_year
01_Male_3_month
04_Male_3_month
03_Male_3_month
02_Male_3_month
2
1
0
-1
-2

D

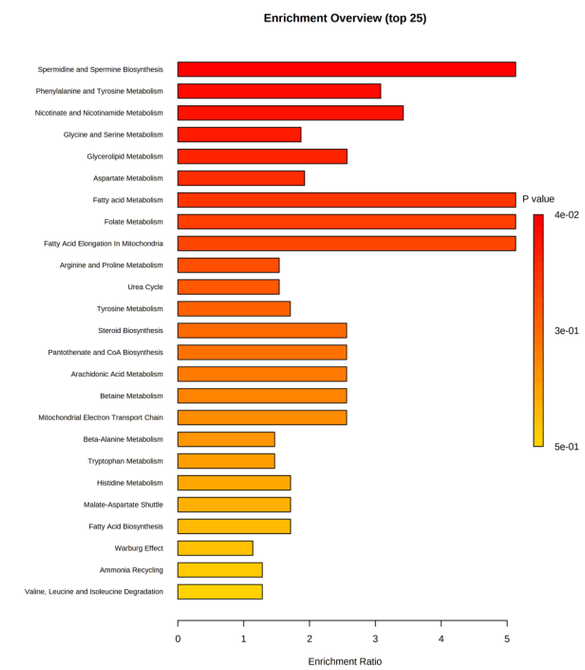
Enrichment Overview (top 25)
Spermidine and Spermine Biosynthesis
Phenylalanine and Tyrosine Metabolism
Nicotinate and Nicotinamide Metabolism
Glycine and Serine Metabolism
Glycerolipid Metabolism
Aspartate Metabolism
Fatty acid Metabolism
Folate Metabolism
Fatty Acid Elongation In Mitochondria
Arginine and Proline Metabolism
Urea Cycle
Tyrosine Metabolism
Steroid Biosynthesis
Pantothenate and CoA Biosynthesis
Arachidonic Acid Metabolism
Betaine Metabolism
Mitochondrial Electron Transport Chain
Beta-Alanine Metabolism
Tryptophan Metabolism
Histidine Metabolism
Malate-Aspartate Shuttle
Fatty Acid Biosynthesis
Warburg Effect
Ammonia Recycling
Valine, Leucine and Isoleucine Degradation
P value
4e-02
3e-01
5e-01
0
1
2
3
4
5
Enrichment Ratio